RSC Advances

PAPER

View Article Online
View Journal | View Issue

Cite this: *RSC Adv.*, 2017, **7**, 41254

Modeling of phase separation across interconnected electrode particles in lithium-ion batteries

Ying Zhao,[a] Luis R. De Jesus,[b] Peter Stein,[a] Gregory A. Horrocks,[b] Sarbajit Banerjee*[b] and Bai-Xiang Xu*[a]

Received 3rd July 2017
Accepted 9th August 2017

DOI: 10.1039/c7ra07352f

rsc.li/rsc-advances

Lithium transport and phase separation in and across interconnected electrode particles are investigated in this paper. This paper signifies the influential role of particle size variation on battery performance with phase-separating electrodes. In this work, a model is developed which accounts for lithium transport in the particles, phase separation, and interface reactions across the particle network. The implementation in 3D is carried out using the B-spline based finite cell method for a straightforward treatment of the Cahn–Hilliard equation and a flexible representation of particle geometry. Representative examples based on scanning transmission X-ray microscopy (STXM) images are simulated to discuss the factors that will influence phase separation during non-equilibrium lithiation and delithiation, as well as relaxation towards equilibrium. The simulations reveal that particles with a slight advance during (de-) lithiation at the beginning will strengthen their advance at the expense of neighboring particles, in a "winner-takes-all" fashion. Moreover, rapid reaction can suppress phase separation, both inside a single particle and across the particle network. Lastly, both particle size and size variation in electrodes composed of phase-separating materials ought to be small to avoid intra- and inter-particle phase separation. This study can serve as a guide for the design of battery electrodes composed of phase-separating materials.

Introduction

Many electrode materials undergo phase transformation and separation upon lithium intercalation, such as $LiFePO_4$, lithium titanate, lithium nickel manganese oxides, V_2O_5, graphite and crystalline silicon (c-Si).[1–10] Such phase separation can be problematic and sometimes destructive to the cyclic electrochemical performance of lithium-ion batteries. Although the volumetric expansion of amorphous silicon (a-Si) is as large as 300% with full lithiation, the homogeneous breathing-like volumetric expansion and contraction alone will not give rise to severe cracks in the particle. Instead, it is the abrupt increase in lithium concentration and tremendous strain mismatch at the c-Si/a-Si interface during the lithiation of c-Si that results in crack propagation and the irreversible capacity fade.[11] Furthermore, phase separation also contributes to the concentrated current in a small number of particles (current "hot-spots"), as reported in the case of $LiFePO_4$.[12]

Considerable phase heterogeneity is also observed for V_2O_5 cathode materials upon lithiation. The layered nature of this compound as well the multiple accessible redox states makes this material an interesting model system for fundamental explorations of intercalation phenomena. Indeed, Raman spectroscopy and powder X-ray diffraction have been used to evaluate the phase evolution of V_2O_5 upon chemical lithiation as a function of particle size.[13] The orthorhombic layered phase of V_2O_5 undergoes a series of intercalation-induced phase transformations with an increasing concentration of inserted Li ions.[14–17] An α-phase, which is slightly distorted from the parent orthorhombic structure, first appears upon the insertion of Li ions and is stabilized for a diminutive composition range of $0 < x < 0.1$ in $Li_xV_2O_5$. Subsequently, an ε-phase nucleates and is the thermodynamically stable polymorph of $Li_xV_2O_5$ in the compositional range of $0.3 < x < 0.85$; the structure is characterized by the initial puckering of the apical oxygens due to their electrostatic interactions with the Li ions and an increase in the inter-layer spacing compared to pristine V_2O_5. Next, a highly puckered δ-phase is stabilized for concentrations of $0.88 < x < 1.0$ in $Li_xV_2O_5$ and is characterized by the sliding of the layers by half a unit cell length along the *b* direction. Indeed, further lithiation above $x > 1.0$ still yields more distorted γ- and ω-phases,[15] however, in these phases the layered V_2O_5 framework is irreversibly transformed and cannot be recovered upon

[a]*Mechanics of Functional Materials Division, Department of Materials Science, TU Darmstadt, Jovanka-Bontschits-Str. 2, 64287 Darmstadt, Germany. E-mail: xu@mfm.tu-darmstadt.de; Fax: +49-6151-16-21034; Tel: +49-6151-16-21906*

[b]*Department of Chemistry, Department of Materials Science and Engineering, Texas A&M University, College Station, TX 77845-3012, USA. E-mail: banerjee@chem.tamu.edu*

delithiation.[18] In contrast, at a low depth of discharge, the transition between the α-, ε-, and δ-phases is entirely reversible.

In previous work, summarized in Table 1, the progression of the phase nucleation of the aforementioned phases in V_2O_5 has been mapped using X-ray diffraction and Raman spectroscopy for different particle sizes: bulk particles (1–10 μm particle size), hydrothermally synthesized nanowires (with diameters of 150–250 nm and lengths spanning multiple microns), and nanoplatelets grown by chemical vapor deposition (20–50 nm).[19] Fig. 1 depicts the electron microscopy images of the three different size distributions. Lithiation of these materials was explored by reacting V_2O_5 with *n*-butyllithium;[20] chemical lithiation has been shown to parallel the phase progression achieved during electrochemical lithiation with high fidelity and allows for evaluation of the lithiation process while eliminating confounding factors such as distance from the electrode and the need for three-point contact in the electrolyte–electrode–conductor.[13] Table 1 summarizes the findings for three different time intervals of lithiation. Upon 1 min of exposure to the lithiating agent, bulk V_2O_5 shows the characteristic signs of the initiation of lithiation: the interior of the sample retains a pristine V_2O_5 character, whereas the surface shows indications of nucleation of the α-phase. In contrast, for the V_2O_5 nanowires the core is transformed to the α-phase, whereas the surface shows indications of nucleation of the ε-phase. The particles with the smallest dimensions, the nanoplatelets, appear to be homogeneously lithiated to the ε-phase. Upon 5 min of chemical lithiation, the bulk samples show a homogeneous α-phase within the core and the surface. For the intermediate size particles, the nanowires, the core is still primarily in the α-phase, whereas the surfaces of the nanowires show signs of ε- and δ-phases. The nanoplatelets with the smallest dimensions show clear signs of the Li-rich ε′-phase. Finally, upon exposure to the lithiating agent for 30 min, the bulk sample shows a core that is completely transformed to the α-phase and a surface with some characteristic signs of the ε-phase. The several hundred nanometer wide nanowires show an interior that is a mix of α- and ε-phases and the nanowire surface is completely transformed to the ε-phase. The smallest particles, the nanoplatelets, are homogeneously transformed to the δ-phase in this time period.[19] These observations, which are summarized in Table 1, clearly illustrate the pronounced influence of particle size on both (i) the kinetics of lithiation and intercalation-induced phase transformations and (ii) phase separation and homogeneity. The α-phase can be readily formed upon the initial lithiation of V_2O_5; however, subsequent phases with higher Li content are stabilized by nucleation and growth through a two-phase regime.[21] There is a monotonic increase in the kinetics of the intercalation-induced phase transformations with decreasing particle size. For the same elapsed time, the smaller particles progress to significantly more Li-rich phases. The particles with the smallest dimensions, the nanoplatelets, show distinctively different behavior which is characterized by homogeneous lithiation without phase separation. Phase

Table 1 Influence of particle size on phase separation upon chemical lithiation of V_2O_5. The phase and extent of lithiation of the particle interiors is determined by powder X-ray diffraction and the phase and extent of lithiation of the particle surfaces is determined by Raman spectroscopy. The three different morphologies of V_2O_5 are compared in Fig. 1

Reaction time interval	Morphology	Interior composition ($Li_xV_2O_5$)	Surface ($Li_xV_2O_5$)	Phase separation
1 minute	Bulk (1–10 μm)	V_2O_5 ($x \sim 0$)	α ($x < 0.1$)	Yes
	Nanowires (150–250 nm)	α ($x < 0.1$)	ε ($0.35 < x < 0.8$)	Yes
	Nanoplatelets (20–50 nm)	ε ($0.35 < x < 0.8$)	ε ($0.35 < x < 0.8$)	No
5 minutes	Bulk (1–10 μm)	α ($x < 0.1$)	α ($x < 0.1$)	No
	Nanowires (150–250 nm)	α ($x < 0.1$)	ε ($0.35 < x < 0.8$) + δ ($0.88 < x < 1.0$)	Yes
	Nanoplatelets (20–50 nm)	ε′ ($x > 0.35$)	ε′ ($x > 0.35$)	No
30 minutes	Bulk (1–10 μm)	α ($x < 0.1$)	α ($x < 0.1$) + ε ($0.35 < x < 0.8$)	Yes
	Nanowires (150–250 nm)	α ($x < 0.1$) + ε ($0.35 < x < 0.8$)	ε ($0.35 < x < 0.8$)	Yes
	Nanoplatelets (20–50 nm)	δ ($0.88 < x < 1.0$)	δ ($0.88 < x < 1.0$)	No

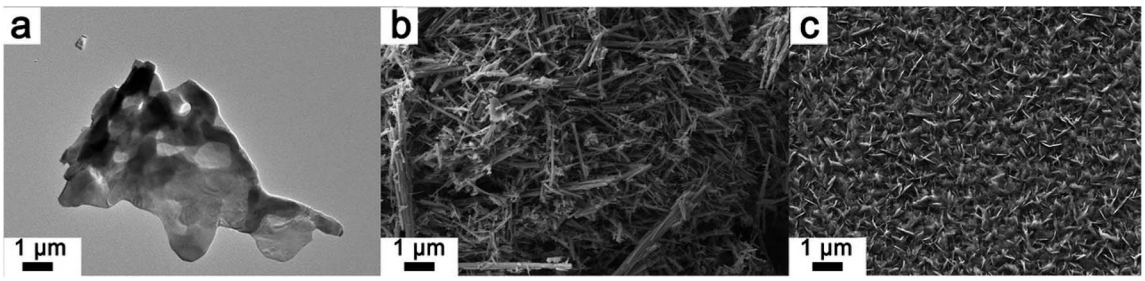

Fig. 1 The three different morphologies of V_2O_5 listed in Table 1: (a) micron-sized powders denoted as bulk, (b) nanowires with lateral dimensions spanning 150–250 nm and spanning tens of microns in length, and (c) nanoplatelets with thicknesses in the range of 20–50 nm.[19] Phase separation is suppressed for the thin nanoplatelets.

separation is clearly size dependent for this system, which shows a pronounced role of dimensionality in modulating Li-ion insertion and extraction. However, the mesoscopic mechanism underpinning such phenomena, which is expected to be widely generalizable to other phase-separating cathode materials, remains to be determined and will indeed be a primary focus of this article. In order to model chemical lithiation, the assumption of a constant global Li-ion flux is most realistic and such a formalism has been used in this work.

Various models have been developed to account for the intercalation-induced phase separation phenomena in electrode materials. Huang *et al.*[22] developed a model that used a flexible sigmoid function to describe the two phase concentration profile with respect to the interface position. In a study by Liu *et al.*,[23] a concentration-dependent diffusion coefficient was introduced in order to describe the sharp Li concentration drop across the interface during lithiation. Zhang *et al.*[24] developed a reaction-controlled diffusion model to account for the bond breaking energy when lithium inserts into c-Si. However, the aforementioned models are either highly empirical and are only applicable in very limited cases, or require sophisticated numerical techniques to track the interface and to re-mesh adaptively.

The phase-field method based on the Cahn–Hilliard equation[25,26] has recently found more applications for lithium diffusion in phase-separating materials, as it requires no tracking of the phase interface. Moreover, it can be tailored for different specific materials, given proper free energy expressions from DFT calculations or from the CALPHAD method.[27] For a qualitative study, the regular solution model[28] is often used to determine the free energy of a binary mixture. The mechanical stress and phase separation in the spherical particles in lithium-ion batteries are discussed in the literature.[29,30] Moreover, the reaction and crack propagation have also been intensively studied in the last several years.[31–36] On the other hand, reaction-limited models based on the Allen–Cahn equation are employed for the simulation of $LiFePO_4$ nanoparticles[37,38] to realize the "domino-cascade" model[13] and to explain the suppression of phase separation at high rates.[39,40]

However, these models are all dealing with single particles and the inter-particle exchange of the Li ions is disregarded. While it is reasonable to assume that single-particle models can reflect multi-particle behaviors in solid-solution systems, they fall short in describing phase-separating systems, as discussed in this article. Ferguson and Bazant developed a porous electrode model, which can describe multi-particle phase-separation behavior.[41] However, in their model, each particle is treated as an effective homogeneous solid solution and the intra-particle phase separation shown in Table 1 is not considered. To account for both the intra- and inter-particle phase separation, a network of particles that can both work independently and communicate with each other is needed. Although there are studies in this regard[42] the connection between the particles is not explicitly considered. Rather, the electrostatic potential drop and the overall current are controlled at the same time in order to implicitly introduce the coupling of two particles without involving actual lithium transport through the electrolyte or across the particle-to-particle interfaces. In this work, the interaction between the particles is explicitly modeled and simulated. The phase-separation behavior within a multi-particle network is then discussed.

Model

A network consisting of several particles in contact with each other is considered in this model. Its 2D illustration with two particles is shown in Fig. 2. The model consists of Cahn–Hilliard bulk diffusion and the Butler–Volmer surface reaction on the electrode/electrolyte, electrode/electrode surfaces.

Diffusion and phase separation in the particles

The lithium diffusion inside each particle p is subject to the Cahn–Hilliard equation

$$\frac{\partial c^{(p)}}{\partial t} = \nabla\cdot\left[M^{(p)}\nabla\left(\mu^{(p)}_{\text{bulk}} - \kappa^{(p)}\nabla^2 c^{(p)}\right)\right] \text{ in } \mathrm{B}^{(p)} \quad (1)$$

where the superscript p value goes from 1 to the total number of particles considered. $\mathrm{B}^{(1)}$ and $\mathrm{B}^{(2)}$ represent the interior of the particle bodies, as shown in Fig. 2. $c^{(p)}$ is the molar concentration normalized with respect to the maximum concentration $c_{\max}$ in each particle, t is the time and M is the mobility, expressed as $Dc_{\max}c^{(p)}(1 - c^{(p)})/(RT)$ in this article. The term $k^{(p)}\nabla^2 c^{(p)}$ represents the interfacial energetic penalty, which disfavors the growth of domain interfaces within a particle. The bulk chemical potential $\mu^{(p)}_{\text{bulk}}$ is based on the regular solution model

$$\mu^{(p)}_{\text{bulk}} = \mu^{0(p)} + RT\left[\ln\left(\frac{c^{(p)}}{1-c^{(p)}}\right) + \chi\left(1-2c^{(p)}\right)\right] \quad (2)$$

where $\mu^{0(p)}$ is the reference chemical potential, R is the gas constant and T is the absolute temperature. The phase parameter χ is taken above 2 to allow for the co-existence of two

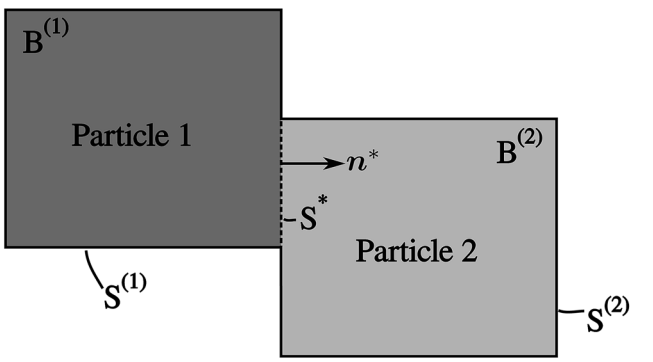

Fig. 2 An illustration of two interconnected particles $\mathrm{B}^{(1)}$ and $\mathrm{B}^{(2)}$. Their surfaces that are exposed to the electrolyte are denoted as $\mathrm{S}^{(1)}$ and $\mathrm{S}^{(2)}$, respectively. The contact surface is denoted as S*, with its normal $\boldsymbol{n}$* facing towards $\mathrm{B}^{(2)}$. The two particles are independent, and the mass transfer between the two particles occurs on the surface S*.

phases. The total chemical potential of the particle p is thus $\mu^{(p)} = \mu^{(p)}_{\text{bulk}} - \kappa^{(p)}\nabla^2 c^{(p)}$.

Reaction on the electrode/electrolyte interface

On the electrode/electrolyte interface, for simplicity, the reaction

$$\text{Li}_{\text{ely}}{}^{+} + \mathscr{H}^{-} \rightleftharpoons \text{Li}\mathscr{H} \tag{3}$$

is considered, with $\mathscr{H}$ being the host material. The lithium influx is given as

$$j_{\text{ely}\to(p)} = c_{\text{s}}^{(p)} R_{\text{BV}}^{(p)} \text{ on } \text{S}^{(p)} \tag{4}$$

in which $c_{\text{s}}^{(p)}$ is the molar concentration of intercalated sites on the surface and R_{BV} is the reaction rate, described by the phenomenological Butler–Volmer equation[39]

$$R_{\text{BV}}^{(p)} = \frac{a_{\text{ely}}{}^{\beta} a_{(p)}{}^{(1-\beta)}}{\tau_0 \gamma_{\text{A}}^{(p)}} \left\{ \exp\left(-\beta \frac{F\eta^{(p)}}{RT} \right) - \exp\left[(1-\beta) \frac{F\eta^{(p)}}{RT} \right] \right\}, \tag{5}$$

where τ_0 is the mean time for a single reaction step and β is a symmetry factor for the forward and backward reactions in eqn (3). The parameter γ_{A} is the chemical activity coefficient of the activated state, expressed as $(1 - c^{(p)})^{-1}$.[39] The overpotential on the surface $\text{S}^{(p)}$ is defined by[33,43]

$$\eta^{(p)} = \mu^{(p)}/F + \Delta\phi^{(p)} - V_{\text{OC}} \tag{6}$$

with $\Delta\phi^{(p)} = \phi^{(p)} - \phi_{\text{ely}}$ being the electrostatic potential difference between the electrode and the electrolyte, and V_{OC} being the open circuit potential. The lithium activity in the particle is defined as $a_{(p)} = \exp[\mu^{(p)}/(RT)]$.

Reaction on the electrode/electrode interface

On the electrode/electrode interface of two interconnected particles, the intercalation of lithium from one particle to another can be considered as the occurrence of the following reaction[44]

$$\text{Li}_{(1)} \rightleftharpoons \text{Li}_{(2)} \tag{7}$$

and, similarly to eqn (4), the particle-to-particle flux can be described by

$$j_{(1)\to(2)} = c_{\text{s}}^{*} R_{\text{BV}}^{*} \quad \text{on} \quad \text{S}^{*} \tag{8}$$

with the reaction rate defined as

$$R_{\text{BV}}^{*} = \frac{a_{(1)}{}^{\beta} a_{(2)}{}^{(1-\beta)}}{\tau_0 \gamma_{\text{A}}^{*}} \left\{ \exp\left(-\beta \frac{F\eta^{*}}{RT} \right) - \exp\left[(1-\beta) \frac{F\eta^{*}}{RT} \right] \right\}. \tag{9}$$

The parameter γ_{A}^{*} is given by $(1 - c^{(1)})^{-1}(1 - c^{(2)})^{-1}$. The two particles are considered to be electronically well connected, therefore the overpotential is purely the difference of the lithium chemical potential in the two particles, *i.e.* $\eta^{*} = (\mu^{(1)} - \mu^{(2)})/F$.

Simulation details

The eqn (1), (4) and (8), together with the initial conditions are solved by the finite element method in three-dimensional space and the backward Euler method in time. In particular, since the Cahn–Hilliard equation is a fourth-order partial differential equation, an additional boundary condition

$$\nabla c^{(p)} \cdot \boldsymbol{n} = 0 \text{ on } \text{S}^{*} \cup \text{S}^{(p)} \tag{10}$$

also needs to be fulfilled. The non-linear equations are solved by the Newton–Raphson iteration method. In order to achieve a flexible description of the particle geometry and a straightforward treatment of the fourth-order partial differential Cahn–Hilliard equation, the B-spline based finite cell method is employed, where the complete network of particles is immersed in a regular background mesh and each particle geometry is represented by integration points. For detailed information, interested readers are referred to the work of Zhao *et al.*[45] All of the codes are implemented in the academic finite element software FEAP.[46]

In the simulation, the particle network is immersed in a lithium bath with a constant potential. The potential drop $\Delta\phi^{(p)}$ is kept constant for a complete (de-)lithiation process. Moreover, since the particles are considered to have equal potential, $\Delta\phi^{(p)}$ is the same for all particles in a single simulation. The simulation parameters are shown in Table 2.

Results and discussion

Phase separation during (de-)lithiation

As the first example, delithiation and lithiation in a two-particle system are investigated. Fig. 3a–d depict scanning transmission X-ray microscopy (STXM) maps of the phase separation of Li-rich and Li-poor domains between two connected V_2O_5 particles that have been chemically lithiated in a lithium bath with a constant potential. The Li content was deduced based on methodology discussed in previous work.[5] Sharp heterogeneity is evident across the interface. In the simulation, the particle geometries are taken from the two V_2O_5 particles in Fig. 3; the larger particle (particle 1) has a size of 20 μm × 0.6 μm × 0.2 μm and the smaller one (particle 2) has a size of 6.8 μm × 0.3 μm × 0.2 μm. The finite element background mesh is quadratic, instead of linear, to capture the interface with fewer elements. The integration points are generated based on an adaptive subdivision to level 3 from the original Cartesian mesh, as shown in Fig. 3e and f. The simulation conditions for the different cases are given in Table 3. The two particles have homogeneous initial concentrations. Upon application of a constant potential drop on the particle surfaces, lithium will flow into/out of the particle during the reaction. At the same time, since the two particles are not lithiated at the same pace due to—for instance—different particle sizes, exchange of lithium across the particles also occurs. In this section, for the sake of convenience, the results of concentration and time are given in their normalized form. Concentration is normalized with respect to the maximum concentration $c_{\max}$, as mentioned previously. Time is normalized by $\tilde{t} = tD/L_0{}^2$. Fig. 4 shows

Table 2 List of parameters

Description	Symbol	Value	Unit	Sources
Gas constant	R	8.32	J mol^{-1} K^{-1}	—
Absolute temperature	T	283	K	—
Faraday's constant	F	96 485	C mol^{-1}	—
Maximum concentration	c_{max}	2.28×10^4	mol m^{-3}	47
Symmetry factor	β	0.5	—	39
Diffusivity	D	1×10^{-12}	cm^2 s^{-1}	47
Length scale	L	1	μm	—
Phase parameter	χ	2.5	—	48
Interfacial parameter	κ		J m^2 mol^{-1}	—
Single reaction step time	τ_0	1	s	47
Lithium activity in electrolyte	a_{ely}	1	—	39
Open circuit potential	V_{OC}	3.4	V	47

a sequence of contour plots of the two-particle system during lithiation (a–d) and delithiation (f–i). During lithiation, instead of being lithiated concurrently, the smaller particle is fully lithiated far before the other particle as shown in Fig. 4c, exhibiting behavior similar to a particle-by-particle transformation. Moreover, the phase change starts from the joint between the two particles (Fig. 4b), indicating that the smaller particle will further extract lithium from the neighboring particle, resulting in an even larger concentration difference and a faster transformation of the smaller particle.[42] This "winner-takes-all" phenomenon is also observed during delithiation: the smaller particle accelerates its delithiation at the cost of the larger one. Fig. 4e and j show plots of the average concentration $\bar{c}(p)$ in each particle during lithiation and delithiation. The average concentration $\bar{c}(p)$ is computed through the equation

$$\bar{c}^{(p)} = \frac{\int_{B^{(p)}} c^{(p)} \mathrm{d}V}{\int_{B^{(p)}} \mathrm{d}V}. \quad (11)$$

The concentration in the two particles bifurcates towards two phases when entering the spinodal region. Curiously, despite the symmetric conditions in the simulation (as shown in Table 3), the fact that delithiation is remarkably slower than lithiation at the beginning indicates that the reaction is non-symmetric. By considering the Butler–Volmer equation (eqn (3)) the reaction is biased by the chemical activity coefficient of the transition state γ_A, which suggests that as lithium occupies more surface sites, it becomes more energetically expensive for the reactants to transit over the activation barrier, thus the reaction becomes slower.[38] The initial concentration in the delithiation process is much higher than that in the lithiation

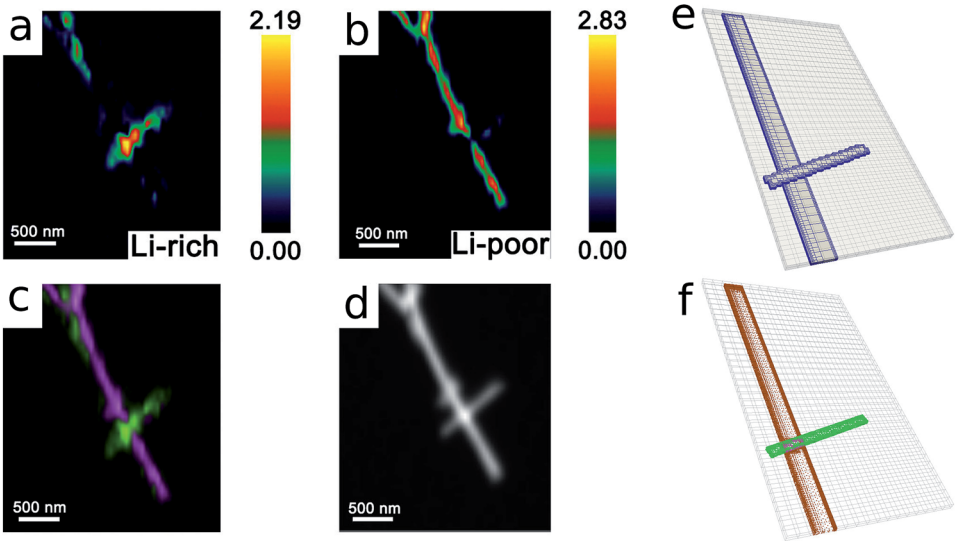

Fig. 3 Compositional mapping of phase separation across two orthogonally connected nanowires based on X-ray microscopy and numerical representation. (a) and (b) map the spatial localization of Li-rich and Li-poor domains, respectively. (c) depicts an overlay of the two domains and (d) is an integrated greyscale intensity image. The assignments of the extent of lithiation are based on methodology discussed in detail in previous work.[5] (e) illustrates the Cartesian background mesh (in black) and the adaptively subdivision (in blue), where the former is the computing grid and the latter is only for calculating the volume integration points. The surface integration points are shown in (f), where the contacting interface S* is shown in magenta and the other surfaces, $S^{(1)}$ and $S^{(2)}$, exposed to the electrolyte are in brown and green, respectively.

Table 3 Different simulated cases. L stands for lithiation and D for delithiation. The comparison between case D1/L1 and case D2/L2 is to stress the influence of the reaction rate on the electrode/electrolyte interface ($c_s^{(p)}$). The comparison between case D1/L1 and case D3/L3 is to show the influence of the connection across the particles (c_s^*). The overpotential is chosen in the simulation so that the lithiation/delithiation will continue until a certain concentration is reached. For a detailed discussion interested readers are referred to the work of Zhao *et al.*[33] and Stein *et al.*[43]

Case	c_{init} (—)	$\Delta\phi - V_{OC}$ (mV)	$c_s^{(p)}$ (mol m^{-2})	c_s^* (mol m^{-2})
D1	0.75	9.76	10^{-7}	10^{-4}
L1	0.25	−9.76	10^{-7}	10^{-4}
D2	0.75	9.76	10^{-4}	10^{-4}
L2	0.25	−9.76	10^{-4}	10^{-4}
D3	0.75	9.76	10^{-7}	0
L3	0.25	−9.76	10^{-7}	0

process, therefore the reaction is much slower in the beginning. However, as time goes on, the reaction rate of the delithiation process overtakes that of the lithiation process since the latter is gradually saturated. For the same reason, the concentration difference between the two particles is larger in the delithiation process than in the lithiation process. In other words, the phase separation is more pronounced during delithiation than during lithiation.[40]

The phase-separation behavior can also be influenced by the reaction rate. Fig. 5 shows the contour plots and the average concentration in the two particles during lithiation and delithiation when the reaction is much faster than the aforementioned case. This is realized numerically by varying the parameter $c_s^{(p)}$ for computational convenience. Experimentally, this can be achieved by a surface treatment on the particle. Alternatively, one can also change the potential difference to attain faster lithiation. From the contour plots we can no longer observe phase separation inside each particle but only a solid-state solution phase. This can be explained by the fact that the influx is so large and quick that it hardly allows particles to equilibrate. Moreover, Fig. 5e and j show that the two particles are almost (de-)lithiated at the same speed, indicating that inter-particle phase separation is also suppressed by fast kinetics of insertion. The phase transformation has been shifted from the particle-by-particle pattern to a concurrent one.[12] It is also observed that, in this case, the concentration difference between the two particles during delithiation is still larger than that during lithiation, which is similar to the previous case.

In the next example, the influence of the interconnectivity between the particles on the phase separation is studied. Fig. 6 shows the simulation results of the scenario where the interaction between the particles is absent. From the contour plots of different time instances we can still observe phase separation in each particle, a phenomenon very much similar to that in the

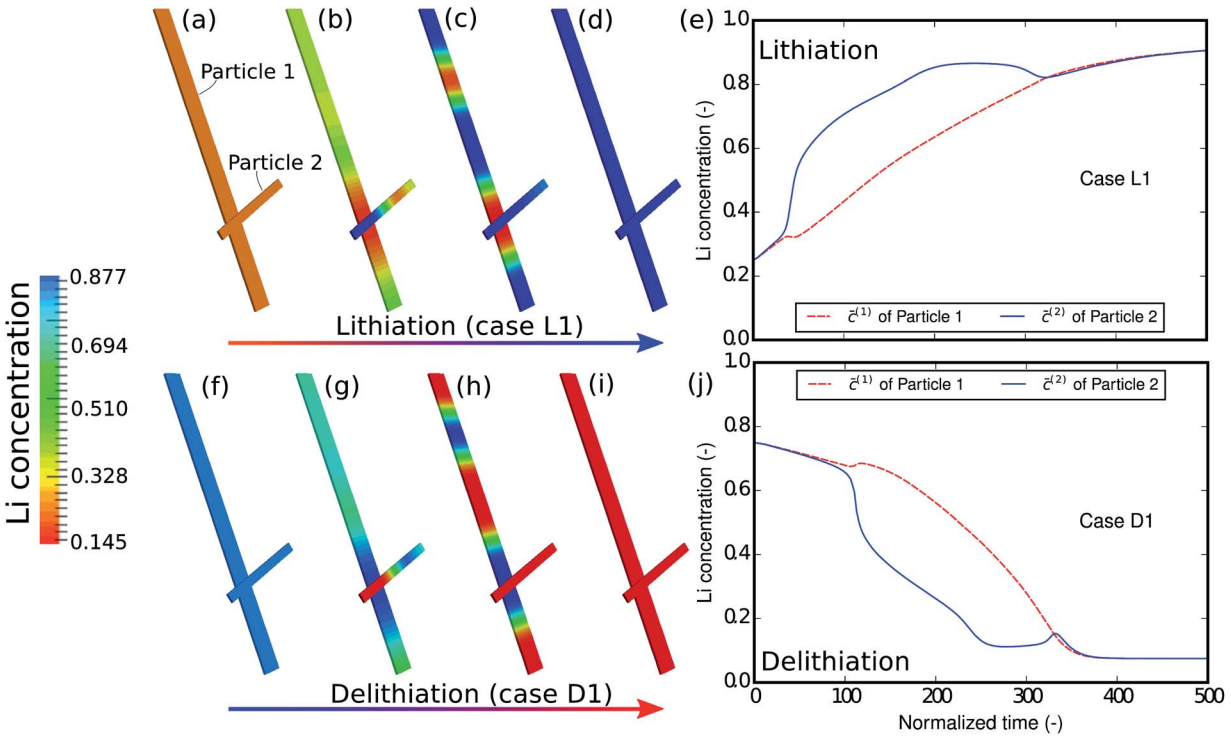

Fig. 4 Contour plots and average concentration in each particle during (a–e) lithiation and (f–j) delithiation for case L1/D1. The simulation conditions for the cases are listed in Table 3. The smaller particle experiences fast phase transformation at the cost of the interconnected particle. The phase separation during delithiation is more significant than during lithiation. (-) in this figure as well as in the following figures stands for the fact that both concentration and time are given in their normalized form. Concentration is normalized with respect to the maximum concentration c_{max} and time is normalized with respect to L_0^2/D.

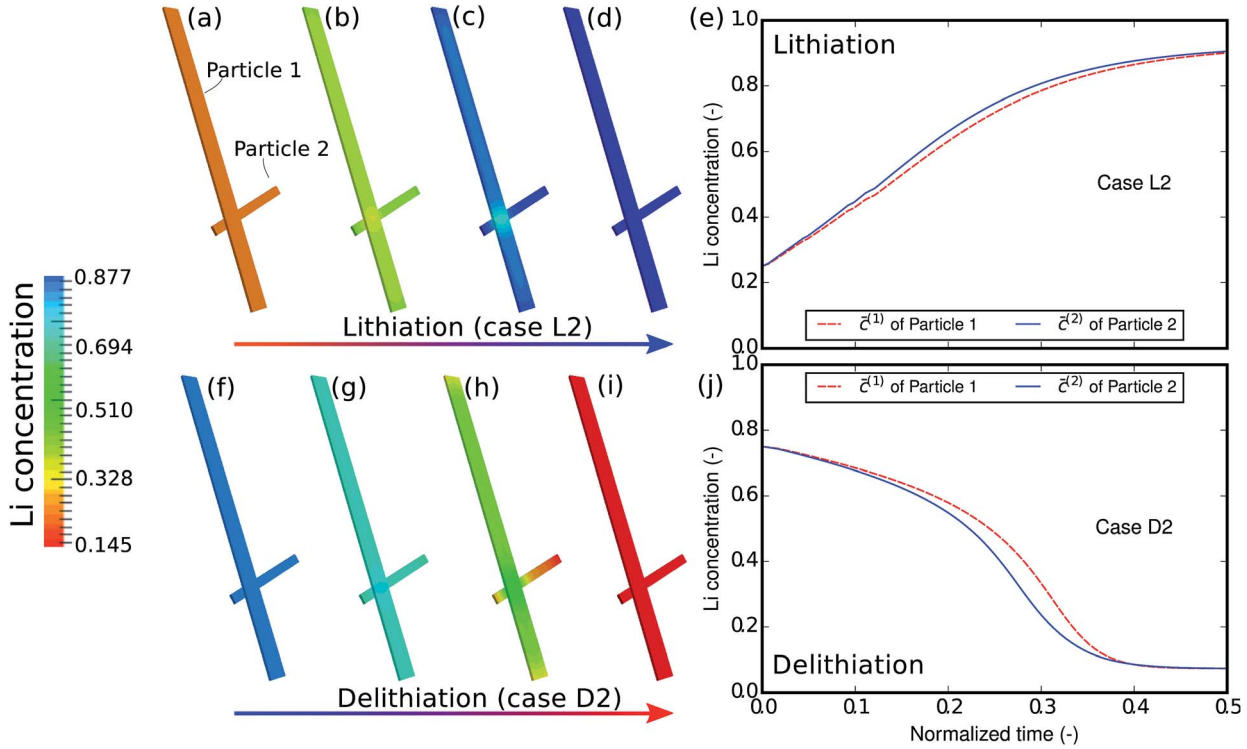

Fig. 5 Contour plots and averaged concentration in each particle during (a–e) lithiation and (f–j) delithiation in case L2/D2. The two particles are lithiated and delithiated at almost the same pace and no inter-particle phase separation occurs.

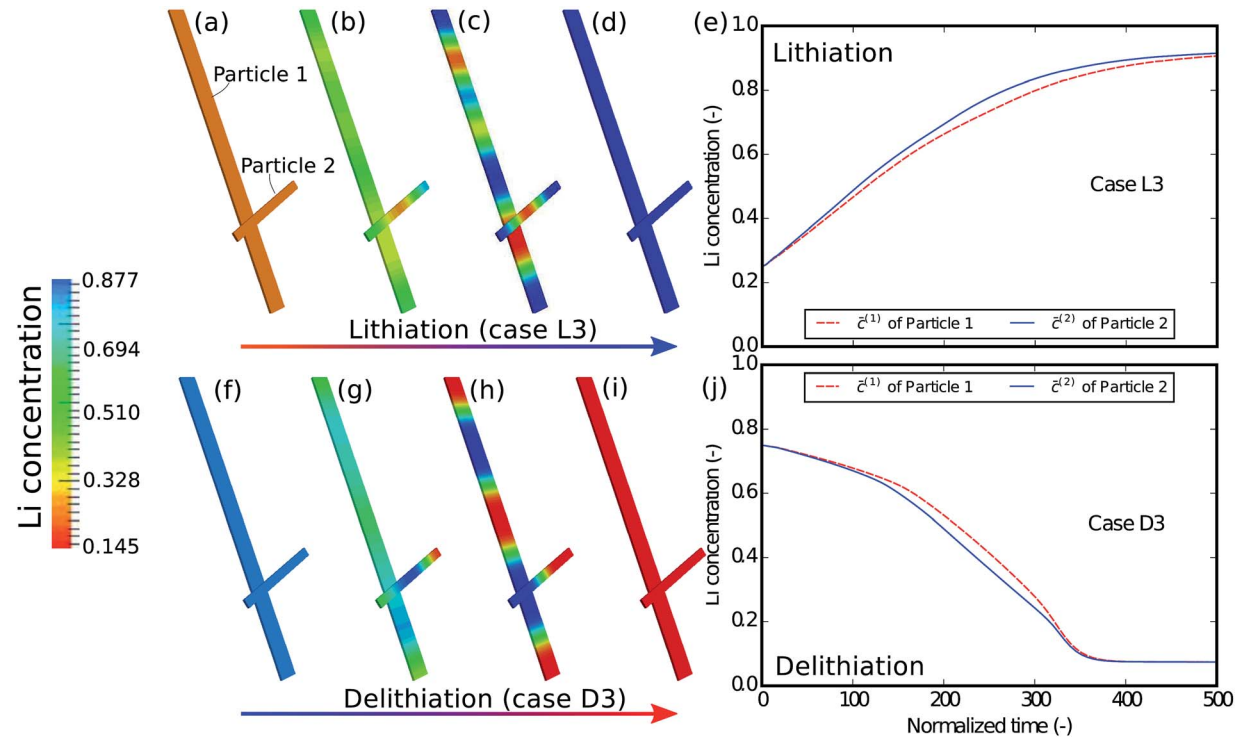

Fig. 6 Contour plots and averaged concentration in each particle during (a–e) lithiation and (f–j) delithiation in case L3/D3, where the inter-connectivity between the particles is absent. The particles are lithiated independently and almost concurrently, which is very different from that in Fig. 4, indicating that a single particle model sometimes cannot exhibit the behavior of a network of multiple particles.

case of D1/L1. However, a more careful comparison between Fig. 4 and 6 shows that only in a well connected network the lithium redistribution starts from the junction of the particles (Fig. 4c), which is also observed in Fig. 3a and b. Moreover, the concentration plots show that, compared to the D1/L1 case, the difference between the two particles is much smaller than that in the D3/L3 case and the two particles are (de-)lithiated almost simultaneously with a slight difference due to the particle size. This indicates that apart from the geometric variations the ionic connectivity also contributes to the phase heterogeneity: the better the connectivity, the stronger the phase heterogeneity. The well established connections between the particles offer a fast pathway for the lithium to equilibrate, allowing the reduction of the phase interfaces within the particle.

Relaxation from the non-equilibrium solid-solution phase

As shown in the previous example and discussed in the literature,[49] at high-rate cycling a non-equilibrium solid-solution is formed with slight compositional variations in different particles. It is thus of interest to evaluate how the relaxation will proceed when the network of particles is charged at different states-of-charge (SOC): will it stay as a solid-solution phase, or will it decompose into different phases? Fig. 7 shows the relaxation of the two-particle network from the initial solid-solution phase with different overall average concentrations c_{ave}s, which represent different SOC. Single-phase diffusion tends to occur when the average amount of lithium is low, as shown in Fig. 7a and e. The particle with higher concentration is willing to bestow lithium to the neighboring particle and a homogenized phase forms across the particles. However, as the lithium content increases to the spinodal region, as shown in Fig. 7b and f, the particle with higher concentration starts to acquire lithium from the neighboring particle in order to globally minimize the energy in the complete network. As a result, instead of blending into one mixture, the concentration in the two particles bifurcates and two distinct phases form. It is worth mentioning that blocking the connection between the particles will prevent the lithium from moving from one particle to another and global energy minimization will not be possible. Thus, inter-particle phase separation will not be observed. If a Li-rich phase already exists in one particle as shown in Fig. 7c and g, a phase transformation will proceed in the other particle, and two phases inside the particle will co-exist. Finally, a homogenized phase appears again when the average concentration is large enough to be out of the spinodal region, as shown in Fig. 7d and h.

Size effect

To understand the size-dependent behavior of the phase separation, particles with different sizes were investigated. The particle sizes are listed in Table 4. The particles were immersed and sparsely distributed in a large lithium bath with a constant potential so that they are neither connected to nor influenced by each other. Fig. 8a shows plots of the respective concentration evolution in each particle. Although the particles are in the same environment, the time for each particle to be fully lithiated varies substantially. In other words, for the same period of time, different particles achieve different levels of lithiation. Apparently, the time for the particle to be fully lithiated increases with increasing particle size. The larger particles have

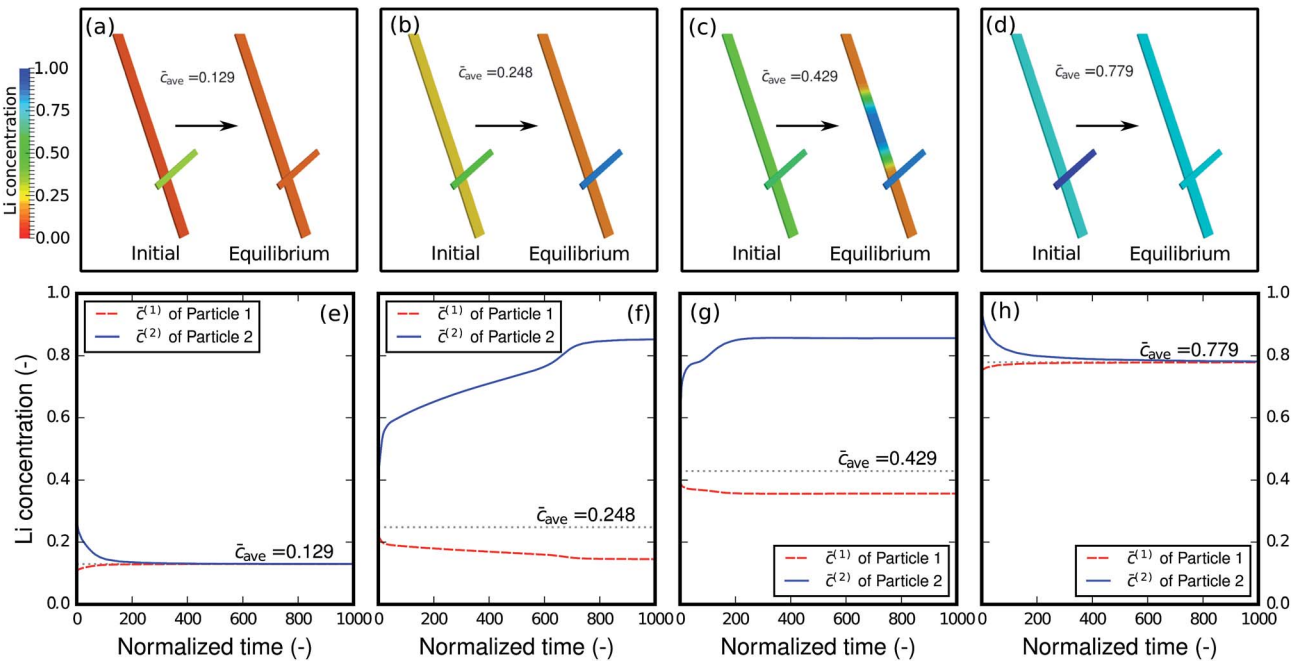

Fig. 7 Relaxation of the two-particle system from the non-equilibrium solid-solution phase with different overall states of charge. Homogeneous phases are reached with very small lithium content (a, e) and very large lithium content (d, h). However, when the overall lithium concentration is within the spinodal region, phase separation between the particles (b, f) and even inside the particles (c, g) occurs.

Table 4 Dimensions of different particles and their respective surface-area-to-volume ratios (S/V) in the study of the size effect. The particles are counted from 3 to distinguish them from the particles discussed in the previous simulations

Particle	Dimensions (μm^3)	S/V (μm^{-1})
3	$20 \times 0.6 \times 0.3$	10.100
4	$10 \times 0.3 \times 0.3$	13.533
5	$3 \times 0.3 \times 0.3$	14.000
6	$1 \times 0.3 \times 0.3$	15.333
7	$0.5 \times 0.3 \times 0.3$	17.333
8	$0.1 \times 0.3 \times 0.3$	33.333

smaller surface-area-to-volume ratios (as shown in Table 4), so they expose less surface per unit volume for the reaction. This explains the "lithium hot-spots" in the network of particles with large size variations.

Moreover, a closer check into the intermediate state of each particle shows that the intra-particle phase-separation behavior is also size dependent. Fig. 8b shows the concentration distribution in the particles at the normalized time instant $\tilde{t} = 100$, when all of the particles are lithiated by around 50% of the total capacity. In the larger particles (3, 4 and 5), phase separation occurs. In particle 3, we can even see patterns of repeated Li-rich and Li-poor phase pairs. It is also worth noting that Li-rich phases always initiate from the ends of the bar-like particles, since there are local high surface-area-to-volume ratios. In the smaller particles (6, 7 and 8), only a solid-solution phase exists. This can be explained by the following two points. Firstly, in smaller particles the reaction-to-diffusion rate is larger, therefore phase separation is more likely to be suppressed, which has been discussed in the D2/L2 case. Secondly, in the small particles, the interfacial mismatch cannot be compensated internally, allowing the interface to grow on to the free surface, thus suppressing phase separation. Based on previous work[48] it is also reasonable to predict that, when the elastic strain is taken into account, the suppression of phase separation will occur even more easily. Since the small particles are almost homogeneous, it is easy to tell that they are at different lithiation stages—the smallest particle is lithiated the most. This agrees very well with Table 1: nanocrystals do not phase separate and medium size nanowires show clear phase separation.

Conclusion

In this study, a model was developed taking into account lithium transport and phase separation inside and across interconnected electrode particles. The model was simulated in 3D with the B-spline based finite cell method. From the representative examples, the following insights are gained.

- In phase-separating materials, particles with a slight advance during lithiation and delithiation at the beginning will strengthen their advance at the cost of the neighboring particle, exhibiting "winner-takes-all" behavior.
- Phase separation—both inside a single particle and across a well connected particle network—is suppressed by rapid intercalation reactions. Moreover, the influence of rapid reactions is more profound during lithiation than during delithiation, representing a non-symmetric reaction.

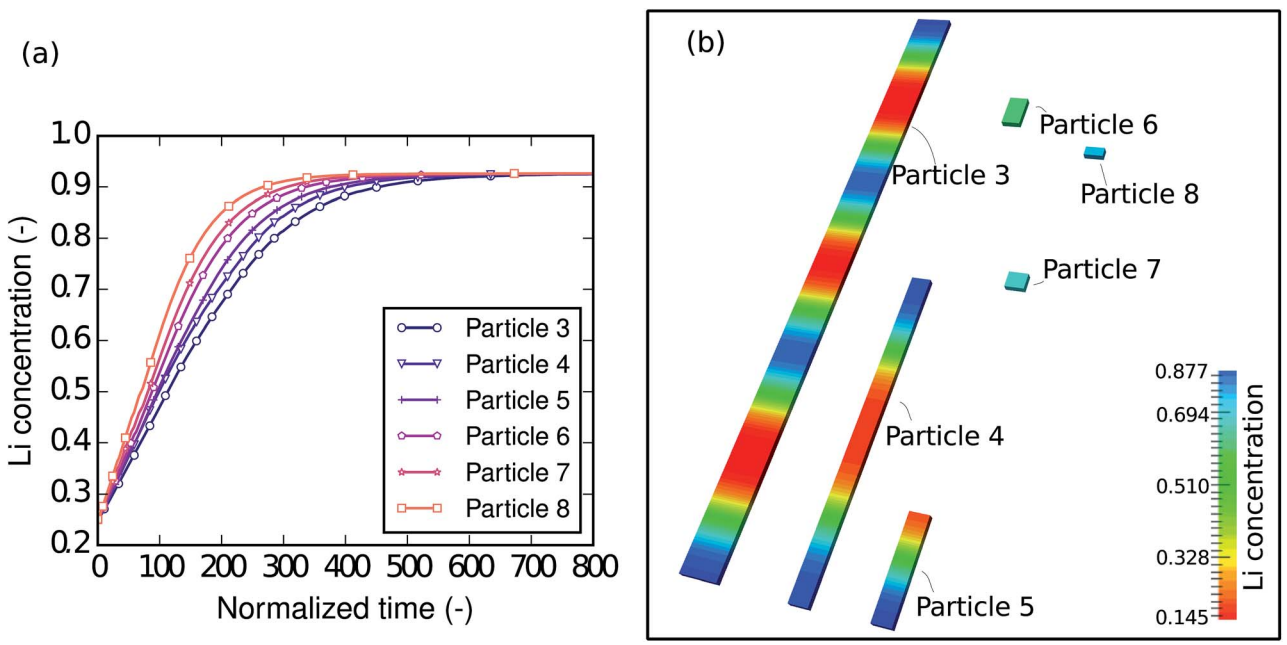

Fig. 8 (a) Plots of lithium concentration versus time during lithiation in particles with different sizes. The smaller particles are lithiated at higher reaction rates thanks to their large surface-area-to-volume ratios. (b) Contour plots of the lithium concentration in particles with different sizes at the normalized time instant $\tilde{t} = 100$. The intra-particle phase separation only takes place in large particles and the Li-rich phases always start from the ends, where there are large local surface-area-to-volume ratios. No phase separation is observed in the small particles (6, 7 and 8).

• Phase separation upon relaxation largely depends on the lithiation state. When the particle network is only slightly or very deeply charged, the homogeneous phase tends to establish itself; when the overall lithiation concentration is in the spinodal region, phase separation is bound to happen.

• Each particle in a network behaves independently as a single particle when the current is large or the ionic connectivity between particles is weak. In either case, the inter-particle mass transfer is not fast enough to equilibrate globally.

• Smaller particles are (de-)lithiated faster than larger particles due to their large surface-area-to-volume ratios. Furthermore, the smaller the particles, the less likely that phase separation inside them will occur.

All of these observations show that, in order to prevent phase separation and the consequent current "hot-spots" in an interconnected particle network, not only particle sizes but also the size variation in electrodes composed of phase-separating materials ought to be made as small as possible.

Conflicts of interest

There are no conflicts to declare.

Acknowledgements

The authors gratefully acknowledge the computing time granted on the Hessian High Performance Computer "Lichtenberg". The author Xu would particularly like to thank the Adolf Messer Foundation for awarding her the Adolf Messer Prize and for financial support. Texas A&M researchers acknowledge support from the National Science Foundation under DMR 1504702. LDJ acknowledges support from the Graduate Research Fellowship under Grant No. 1252521.

References

1 C. Daniel and J. O. Besenhard, *Handbook of Battery Materials*, Wiley-VCH, Weinheim, 2nd edn, 2011.
2 M. T. McDowell, I. Ryu, S. W. Lee, C. Wang, W. D. Nix and Y. Cui, *Adv. Mater.*, 2012, **24**, 6034–6041.
3 A. Van der Ven, C. Marianetti, D. Morgan and G. Ceder, *Solid State Ionics*, 2000, **135**, 21–32.
4 W.-J. Zhang, *J. Power Sources*, 2011, **196**, 877–885.
5 L. R. D. Jesus, G. A. Horrocks, Y. Liang, A. Parija, C. Jaye, L. Wangoh, J. Wang, D. A. Fischer, L. F. J. Piper, D. Prendergast and S. Banerjee, *Nat. Commun.*, 2016, **7**, 12022.
6 J.-J. Xu, Q.-C. Liu, Y. Yu, J. Wang, J.-M. Yan and X.-B. Zhang, *Adv. Mater.*, 2017, **29**, 1606552.
7 H. Zhong, J. Wang, F. Meng and X. Zhang, *Angew. Chem., Int. Ed.*, 2016, **55**, 9937–9941.
8 F. Meng, H. Zhong, D. Bao, J. Yan and X. Zhang, *J. Am. Chem. Soc.*, 2016, **138**, 10226–10231.
9 H.-X. Zhong, K. Li, Q. Zhang, J. Wang, F.-L. Meng, Z.-J. Wu, J.-M. Yan and X.-B. Zhang, *NPG Asia Mater.*, 2016, **8**, e308.
10 J. Wang, H.-X. Zhong, Z.-L. Wang, F.-L. Meng and X.-B. Zhang, *ACS Nano*, 2016, **10**, 2342–2348.
11 J. Rohrer and K. Albe, *J. Phys. Chem. C*, 2013, **117**, 18796–18803.
12 Y. Li, F. El Gabaly, T. R. Ferguson, R. B. Smith, N. C. Bartelt, J. D. Sugar, K. R. Fenton, D. A. Cogswell, A. L. D. Kilcoyne, T. Tyliszczak, M. Z. Bazant and W. C. Chueh, *Nat. Mater.*, 2014, **13**, 1149–1156.
13 C. Delmas, M. Maccario, L. Croguennec, F. Le Cras and F. Weill, *Nat. Mater.*, 2008, **7**, 665–671.
14 N. A. Chernova, M. Roppolo, A. C. Dillon and M. S. Whittingham, *J. Mater. Chem.*, 2009, **19**, 2526–2552.
15 M. S. Whittingham, *Chem. Rev.*, 2004, **104**, 4271–4302.
16 C. Satto, P. Sciau, E. Dooryhee, J. Galy and P. Millet, *J. Solid State Chem.*, 1999, **146**, 103–109.
17 J. Galy, *J. Solid State Chem.*, 1992, **100**, 229–245.
18 R. J. Cava, A. Santoro, D. W. Murphy, S. M. Zahurak, R. M. Fleming, P. Marsh and R. S. Roth, *J. Solid State Chem.*, 1986, **65**, 63–71.
19 G. A. Horrocks, M. F. Likely, J. M. Velazquez and S. Banerjee, *J. Mater. Chem. A*, 2013, **1**, 15265–15277.
20 M. S. Whittingham and M. B. Dines, *J. Electrochem. Soc.*, 1977, **124**, 1387–1388.
21 G. A. Horrocks, E. J. Braham, Y. Liang, L. R. De Jesus, J. Jude, J. M. Velázquez, D. Prendergast and S. Banerjee, *J. Phys. Chem. C*, 2016, **120**, 23922–23932.
22 S. Huang, F. Fan, J. Li, S. Zhang and T. Zhu, *Acta Mater.*, 2013, **61**, 4354–4364.
23 X. H. Liu, L. Zhong, S. Huang, S. X. Mao, T. Zhu and J. Y. Huang, *ACS Nano*, 2012, **6**, 1522–1531.
24 X. Zhang, S. W. Lee, H.-W. Lee, Y. Cui and C. Linder, *Extreme Mech. Lett.*, 2015, **4**, 61–75.
25 J. W. Cahn and J. E. Hilliard, *J. Chem. Phys.*, 1958, **28**, 258–267.
26 J. W. Cahn, *Acta Metall.*, 1961, **9**, 795–801.
27 L.-Q. Chen, *Annu. Rev. Mater. Res.*, 2002, **32**, 113–140.
28 E. Guggenheim, *Mixtures: The Theory of the Equilibrium Properties of Some Simple Classes of Mixtures Solutions and Alloys*, Clarendon Press, 1952.
29 M. Huttin and M. Kamlah, *Appl. Phys. Lett.*, 2012, **101**, 133902.
30 E. Bohn, T. Eckl, M. Kamlah and R. McMeeking, *J. Electrochem. Soc.*, 2013, **160**, A1638–A1652.
31 C. V. Di Leo, E. Rejovitzky and L. Anand, *Int. J. Solids Struct.*, 2015, **67–68**, 283–296.
32 C. Miehe, H. Dal, L.-M. Schänzel and A. Raina, *Int. J. Numer. Meth. Eng.*, 2016, **106**, 683–711.
33 Y. Zhao, B.-X. Xu, P. Stein and D. Gross, *Comput. Meth. Appl. Mech. Eng.*, 2016, **312**, 428–446.
34 B.-X. Xu, Y. Zhao and P. Stein, *GAMM-Mitteilungen*, 2016, vol. 39, pp. 92–109.
35 M. Klinsmann, D. Rosato, M. Kamlah and R. M. McMeeking, *J. Electrochem. Soc.*, 2016, **163**, A102–A118.
36 P. Barai and P. P. Mukherjee, *J. Electrochem. Soc.*, 2016, **163**, A1120–A1137.
37 G. K. Singh, G. Ceder and M. Z. Bazant, *Electrochim. Acta*, 2008, **53**, 7599–7613.
38 M. Z. Bazant, *Acc. Chem. Res.*, 2013, **46**, 1144–1160.

39 P. Bai, D. A. Cogswell and M. Z. Bazant, *Nano Lett.*, 2011, **11**, 4890–4896.
40 J. Lim, Y. Li, D. H. Alsem, H. So, S. C. Lee, P. Bai, D. A. Cogswell, X. Liu, N. Jin, Y.-s. Yu, N. J. Salmon, D. A. Shapiro, M. Z. Bazant, T. Tyliszczak and W. C. Chueh, *Science*, 2016, **353**, 566–571.
41 T. R. Ferguson and M. Z. Bazant, *J. Electrochem. Soc.*, 2012, **159**, A1967–A1985.
42 B. Orvananos, H.-C. Yu, A. Abdellahi, R. Malik, C. P. Grey, G. Ceder and K. Thornton, *J. Electrochem. Soc.*, 2015, **162**, A965–A973.
43 P. Stein, Y. Zhao and B.-X. Xu, *J. Power Sources*, 2016, **332**, 154–169.
44 N. Sato, *Electrochemistry at Metal and Semiconductor Electrodes*, Elsevier Science, Amsterdam, 1998.
45 Y. Zhao, D. Schillinger and B.-X. Xu, *J. Comput. Phys.*, 2017, **340**, 177–199.
46 R. L. Taylor, *FEAP – Finite Element Analysis Program*, 2014.
47 B. Orvananos, T. R. Ferguson, H.-C. Yu, M. Z. Bazant and K. Thornton, *J. Electrochem. Soc.*, 2014, **161**, A535–A546.
48 Y. Zhao, P. Stein and B.-X. Xu, *Comput. Meth. Appl. Mech. Eng.*, 2015, **297**, 325–347.
49 H. Liu, F. C. Strobridge, O. J. Borkiewicz, K. M. Wiaderek, K. W. Chapman, P. J. Chupas and C. P. Grey, *Science*, 2014, **344**, 1252817.